

A Reproducible and Physically Feasible Dynamic Parameter Identification Framework for a Low-Cost Robot Arm

Junji Oaki, Koki Yamane, Koki Inami, and Sho Sakaino

Abstract—This paper presents a reproducible and physically feasible dynamic parameter identification framework for CRANE-X7, a low-cost robot arm driven by modular smart actuators. To improve practical identifiability, products of inertia are removed according to approximate link symmetry, reducing the rigid-body model from 65 to 39 base parameters. Identification motions are hand-designed from structured single-joint and adjacent-joint primitives under practical joint-range limits. The proposed pipeline combines preprocessing, inverse-dynamics-regressor-based ordinary least squares (OLS), conditional semidefinite-programming (SDP) projection for feasibility recovery, and closed-loop input error (CLIE) refinement. Candidate solutions from 40 structured trajectories are analyzed in a common principal component analysis (PCA) space to select a statistically central representative model. Because statistical centrality alone does not ensure physical acceptability, the selected model is finally screened by an all-pose positive-definiteness audit of the inertia matrix and, when necessary, corrected by a localized post-CLIE SDP rescue step. Experiments show that the parameter cloud becomes progressively more concentrated from OLS to SDP and CLIE, while the final accepted model preserves high predictive accuracy on held-out validation motions. These results demonstrate a practical route to statistically coherent and physically feasible dynamic models for low-cost robot platforms.

Index Terms—Dynamic parameter identification, low-cost robot arm, base parameters, physical feasibility, positive definiteness, structured excitation trajectories

I. INTRODUCTION

LOW-COST robot manipulators are becoming increasingly important as research platforms for teleoperation, data collection, and imitation learning. Open low-cost manipulation platforms such as ALOHA and ALOHA 2 have accelerated large-scale teleoperation and imitation-learning research, partly by combining accessible hardware with reproducible data-collection procedures [1], [2]. Many such platforms rely on compact modular smart actuators such as ROBOTIS DYNAMIXEL X-series devices, which support current-based operation and daisy-chain communication but also introduce limited sensing resolution, communication delay, and drivetrain nonidealities. The CRANE-X7 platform used in this study is a representative low-cost arm based on DYNAMIXEL X-series actuators [3], [4], and recent studies have demonstrated its practical use in bilateral-control-based manipulation, motion modification, and sensorless teleoperation [5]–[7].

Dynamic parameter identification on low-cost robot arms remains challenging. Compared with industrial manipulators,

the sensing resolution is limited, communication and realization delays are not negligible, and drivetrain nonidealities such as backlash-related effects are more pronounced. As a result, straightforward identification with a high-dimensional rigid-body model is often numerically fragile and may produce parameter sets that fit measured torque data well but remain physically implausible over a broader pose range.

Classical studies established that robot dynamics can be expressed linearly with respect to inertial parameters and that only a reduced set of base parameters is structurally identifiable [8]–[10]. Subsequent work addressed physical feasibility and positive-definiteness recovery through constrained formulations such as linear matrix inequalities and semidefinite programming [11]–[13]. Closed-loop and output-error/input-error methods further improved predictive performance in robot identification [14]–[16], while symbolic tools such as OpenSYMORO improved the reproducibility of model and regressor generation [17]. However, a compact framework that combines these ideas for a low-cost robot arm, while explicitly screening the final model for broad-range physical acceptability, is still lacking.

This paper presents a reproducible and physically feasible dynamic parameter identification framework for CRANE-X7. Instead of using numerically optimized excitation trajectories, the candidate identification motions are hand-designed from structured single-joint and adjacent-two-joint primitives under practical joint-range limits, following the classical insight that informative manipulator tests can be organized from simple motion patterns [8], [18]. To improve conditioning and reproducibility, the products of inertia are set to zero according to the approximate link symmetry of the platform, reducing the model dimension from 65 to 39 parameters. The identification pipeline combines preprocessing, inverse dynamics identification model (IDIM) regressor construction using OpenSYMORO, ordinary least squares (OLS), semidefinite programming (SDP), and closed-loop input error (CLIE) refinement. Candidate solutions obtained from 40 structured trajectories are then evaluated statistically in principal component analysis (PCA) space and screened by an all-pose positive-definiteness audit of the inertia matrix.

The main contribution is a staged identification framework matched to the practical constraints of a low-cost robot arm. The experiments show that the parameter cloud becomes progressively more concentrated from OLS to SDP and further to CLIE, while also revealing that torque-fitting accuracy alone is insufficient to guarantee physical feasibility. A representative candidate selected from the final cloud is therefore subjected to a final positive-definiteness-based rescue step and evaluated on held-out validation motions.

Junji Oaki, Koki Yamane, Koki Inami, and Sho Sakaino are with the Institute of Systems and Information Engineering, University of Tsukuba, 1-1-1 Tennodai, Tsukuba, Ibaraki 305-8573, Japan (email: oaki.junji.fu@u.tsukuba.ac.jp)

II. RELATED WORK

Classical robot dynamic identification established inverse-dynamics regressors, least-squares estimation, and base-parameter representations [8]–[10], [19]. These results provide the structural basis for the reduced regressor used here, while symbolic tools such as OpenSYMORO improve reproducibility by generating robot-specific dynamic models and regressors [17].

Excitation design has been studied using information criteria, condition numbers, and optimized Fourier or polynomial trajectories [20]–[24]. These designs are powerful when accurately executable, but low-cost platforms impose practical limits through delay, finite encoder resolution, and drivetrain imperfections. The present work therefore uses interpretable single-joint and adjacent-joint primitives, consistent with classical accelerated test motions [8], [18].

Physical feasibility has been addressed by positive-definiteness checks, linear matrix inequalities, semidefinite programming, and related consistency conditions [11]–[13], [25]–[27]. Related mechatronic robot studies include Lie-theory-based identification, optimal information methods, and model-based control using identified parameters [27]–[30], supporting the view that torque fitting alone is insufficient when the model is used for simulation or control.

Closed-loop and output-error/input-error methods, including closed-loop output error (CLOE), CLIE, and the direct and inverse dynamic identification model (DIDIM), account for realized closed-loop behavior [14]–[16], [31]. Physically consistent DIDIM (PC-DIDIM) avoids unreliable direct simulation from physically infeasible intermediate estimates [32], but typically benefits from a CAD/CAE-initialized standard inertial-parameter representation. In contrast, this study starts from data-driven OLS estimates in the OpenSYMORO base-parameter space without CAD inertial parameters.

Recent studies on Franka Emika Panda, KUKA iiwa, Universal Robot UR5, and the da Vinci Research Kit demonstrate the need for feasible identified models in predictive control and simulation [33]–[36]. In parallel, CRANE-X7, ALOHA, and ALOHA 2 highlight the growing need for reproducible modeling on low-cost hardware [1]–[3], [5]–[7]. The present work combines these strands into a no-CAD pipeline tailored to low-cost manipulators.

III. ROBOT SYSTEM AND DYNAMIC MODELING

A. CRANE-X7 Platform

The experimental platform used in this study was CRANE-X7, a low-cost 7-degree-of-freedom serial robot arm equipped with a one-degree-of-freedom hand axis. Figure 1 shows the CRANE-X7 platform and the modified DH parameter setting adopted for symbolic model generation. The posture shown in Fig. 1 is defined by $\theta_1 = \theta_2 = \theta_3 = \theta_5 = \theta_6 = \theta_7 = 0^\circ$ and $\theta_4 = -90^\circ$, and was used as the nominal posture for the joint-level realization model introduced below.

Despite its flexibility as a research platform, CRANE-X7 presents several challenges for dynamic parameter identification: 12-bit link-side encoders, communication delay and jitter, and realized joint behavior that deviates from the ideal

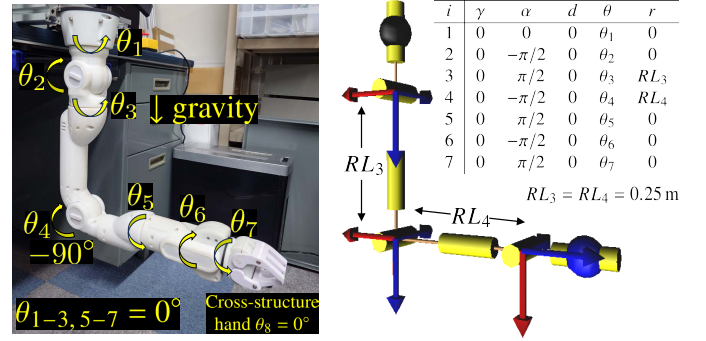


Fig. 1. CRANE-X7 with the replaced cross-structure hand [5] and its kinematic settings using the modified Denavit-Hartenberg (DH) parameterization.

torque source assumed in industrial robot identification. All eight axes were driven by ROBOTIS DYNAMIXEL X-series actuators connected through an RS485 daisy chain [4]. Axes 1 and 3–8 used XM430-W350 actuators, whereas Axis 2 used an XM540-W270 actuator. The current-to-torque conversion constants used in this study were 2.3179 N m/A for the XM430-W350 actuators and 3.1317 N m/A for the XM540-W270 actuator. The torque records used for identification were obtained from the actuator current values using these conversion constants. The robot was operated in current-command mode from a Linux PC, which enabled torque-level control and model-based motion generation. As a result, high-gain feedback alone is insufficient for repeatable identification motions, motivating a model-assisted motion-realization layer.

B. Joint-Level Modeling and Identification

Before performing full rigid-body parameter identification, a simplified joint-level model is introduced for each axis to enable stable and reproducible execution of the structured excitation trajectories.

Figure 2 summarizes the joint-level modeling and identification used for FF+PD controller design. The joint-level identification used an open-loop square-wave and pseudo-random binary sequence (PRBS) input, and the output velocity was obtained by encoder differencing. For the representative Joint 7 response, a first-order-plus-dead-time model was fitted in MATLAB using `procest`. A fourth-order autoregressive model with exogenous input (ARX) was also identified from the same data and used only for frequency-response comparison. The comparison shows that the simplified model captures the low-frequency behavior needed for motion realization, whereas the ARX response reveals higher-frequency discrepancies associated with backlash-related dynamics.

The joint dynamics are modeled as

$$G_j(s) = \frac{K_{p,j}}{1 + T_{p1,j}s} \exp(-T_{d,j}s), \quad (1)$$

where $K_{p,j}$, $T_{p1,j}$, and $T_{d,j}$ denote the low-frequency gain, time constant, and effective dead time of Joint j , respectively.

For Joint 7, the identified parameters were $K_{p,7} = 25.0$, $T_{p1,7} = 0.15$, and $T_{d,7} = 0.0015$.

The identified dead time is consistent with the realization layer of the platform. Reading all eight encoder values and

TABLE I
REDUCED 39-PARAMETER STRUCTURE USED FOR CRANE-X7 DYNAMIC IDENTIFICATION.

Group	Parameter type	Unit	Count
Link-side	Inertia base terms	kg m ²	13
Link-side	First-moment base terms	kg m	12
Motor-side	Rotor inertia terms	kg m ²	6
Joint-side	Viscous friction terms	N m s/rad	8
Reduced model total			39
Original symbolic model			65

issuing current commands introduces a communication delay of approximately 900 μ s. Under the 1 ms control cycle, the sample-and-hold effect contributes an additional delay of approximately 500 μ s, resulting in a total delay of about 1.5 ms.

Similar first-order-plus-dead-time models were obtained for the other joints in the relevant frequency range. Although higher-order dynamics such as backlash-induced modes around 100 Hz exist, they are not explicitly modeled in the robot-level identification framework.

Using this realization-oriented model, the structured excitation trajectories are executed by a fixed feedforward plus PD controller with pseudo differentiation. The pseudo-differentiated velocity is defined as $\hat{\theta} = \frac{s}{1+T_f s} \theta$ with $T_f = 0.002$, and the realization-oriented command is written as

$$u_{\text{FF+PD}} = \hat{M} \left[K_V \left(\dot{\theta}_{\text{ref}} + K_P K_V^{-1} (\theta_{\text{ref}} - \theta) - \hat{\theta} \right) + \ddot{\theta}_{\text{ref}} \right] + \hat{D} \dot{\theta}_{\text{ref}}. \quad (2)$$

Here, K_P and K_V are diagonal proportional and velocity gains, and \hat{M} and \hat{D} are realization parameters obtained from the joint-level modeling. These parameters serve only for motion realization and should not be interpreted as the final robot-level dynamic parameters.

C. Reduced Rigid-Body Dynamic Model

The robot-level parameter identification is performed using the following reduced rigid-body model:

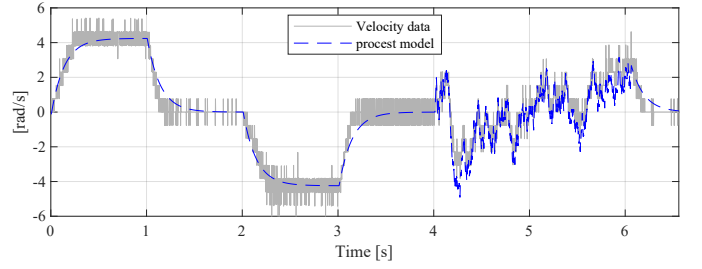
$$\tau = M(\theta) \ddot{\theta} + C(\theta, \dot{\theta}) \dot{\theta} + g(\theta) + f_v(\dot{\theta}), \quad (3)$$

where τ is the joint torque vector, $M(\theta)$ is the inertia matrix, $C(\theta, \dot{\theta}) \dot{\theta}$ represents Coriolis and centrifugal effects, $g(\theta)$ is the gravity term, and $f_v(\dot{\theta})$ denotes viscous friction.

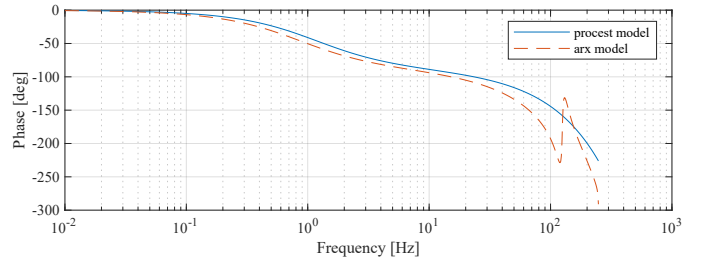
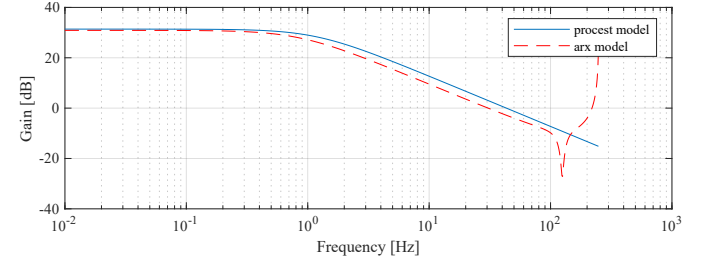
Only viscous friction is retained in the identified model. This choice avoids absorbing quantization, timestamp fluctuations, communication delays, and drivetrain imperfections into a more flexible friction model, and keeps the identified model interpretable and reproducible.

The symbolic model and regressor are generated using OpenSYMORO. While the full inertia-tensor model contains 65 parameters, the reduced model contains 39 base parameters, consisting of 25 link-side terms, 6 motor-side inertia terms, and 8 viscous-friction coefficients.

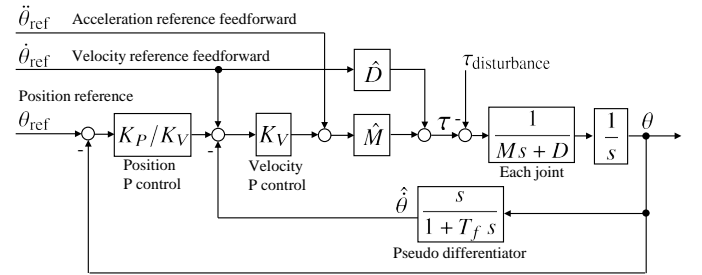
Table I summarizes the reduced parameter structure. The 25 link-side terms consist of 13 inertia-related base terms and 12 first-moment base terms after removing the products of inertia



(a) velocity response vs first-order-plus-dead-time model response



(b) frequency responses of the fourth-order ARX and first-order-plus-dead-time models



(c) fixed FF+PD controller with pseudo differentiation

Fig. 2. Joint-level modeling and identification for FF+PD controller design.

according to the approximate link symmetry of CRANE-X7. The complete parameter names and final numerical values are listed in Appendix A. In the reduced parameterization, inertia-related terms without the prefix M have units of kg·m², whereas the M -prefixed first-moment terms have units of kg·m. The viscous friction coefficients have units of N·m·s/rad.

IV. DYNAMIC PARAMETER IDENTIFICATION FRAMEWORK

Hereafter, PD in phrases such as all-pose PD audit, PD-feasible projection, and PD rescue denotes positive definiteness of the inertia matrix, whereas proportional-derivative control appears only in the controller notation FF+PD.

The joint-level models introduced in Sec. III are used only to realize the structured excitation trajectories reproducibly on the CRANE-X7 platform. The actual dynamic parameter identification is performed at the robot level using the reduced

rigid-body model in (3). Based on this model, the proposed method is formulated as a multi-stage pipeline consisting of IDIM-based linear regression, ordinary least squares (OLS), conditional semidefinite-programming (SDP)-based feasible projection, and closed-loop input error (CLIE) refinement. Since the resulting estimates still depend on the excitation set, the final parameter cloud is further analyzed through principal component analysis (PCA), from which a statistically central candidate is selected and finally screened by the all-pose PD criterion.

A. IDIM-Based Linear Regression

Starting from the reduced rigid-body model in (3), the inverse dynamics are rewritten in a form that is linear in the unknown reduced parameter vector ϕ :

$$\tau = \mathbf{W}(\theta, \dot{\theta}, \ddot{\theta}) \phi, \quad (4)$$

where $\mathbf{W}(\theta, \dot{\theta}, \ddot{\theta})$ is the inverse dynamic identification matrix generated from the symbolic rigid-body model, and ϕ is the reduced base-parameter vector.

In the present study, the symbolic regressor is constructed using OpenSYMORO, specifically from its dynamic identification model output `dim.txt`, so that model generation remains reproducible and consistent with the reduced parameterization described in Sec. III.

For each identification trajectory, the measured joint motion and torque data are first preprocessed by anti-aliasing, time alignment, and resampling, and are then substituted into (4). By stacking all samples from a given identification run, the regression model is written as

$$\tau_{\text{all}} = \mathbf{W}_{\text{all}} \phi + \varepsilon, \quad (5)$$

where τ_{all} is the stacked torque vector, \mathbf{W}_{all} is the stacked regressor, and ε is the residual vector. This stacked form provides the common linear starting point for all subsequent stages.

B. OLS Estimation and Conditional SDP-Based Feasible Projection

The initial reduced-parameter estimate is obtained by ordinary least squares:

$$\hat{\phi}_{\text{OLS}} = \arg \min_{\phi} \|\tau_{\text{all}} - \mathbf{W}_{\text{all}} \phi\|_2^2. \quad (6)$$

Equivalently, the closed-form solution is

$$\hat{\phi}_{\text{OLS}} = (\mathbf{W}_{\text{all}}^T \mathbf{W}_{\text{all}})^{-1} \mathbf{W}_{\text{all}}^T \tau_{\text{all}}. \quad (7)$$

This estimate serves as the reproducible linear baseline of the proposed framework. After obtaining $\hat{\phi}_{\text{OLS}}$, an all-pose PD audit is first applied to the OLS solution itself. If the OLS solution already satisfies the all-pose PD criterion, it is passed directly to the CLIE stage. Otherwise, an SDP-based feasible projection is applied before CLIE. When the OLS solution is non-PD, the projection is written as

$$\begin{aligned} \hat{\phi}_{\text{SDP}} &= \arg \min_{\phi} \left\| \phi - \hat{\phi}_{\text{OLS}} \right\|_2^2 \\ \text{s.t. } & \mathbf{M}(\theta; \phi) \succeq \varepsilon_{\text{PD}} \mathbf{I}, \quad \forall \theta \in \Theta, \end{aligned} \quad (8)$$

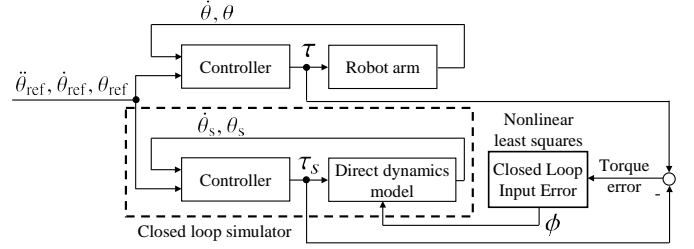


Fig. 3. Closed-loop input error (CLIE) refinement. A candidate parameter vector is evaluated through a closed-loop forward-dynamics simulation using the same fixed FF+PD controller as in the experiment. The simulated controller input torque is compared with the measured torque, and the parameter vector is updated by nonlinear least squares.

where Θ denotes the joint-space domain used in the all-pose audit, \mathbf{I} is the identity matrix, and ε_{PD} is the positive-definiteness margin used in the SDP projection.

In the present study, ε_{PD} was selected from the discrete set $\{0.001, 0.002, 0.005, 0.01\}$, and the smallest value yielding a PD-feasible projection was adopted for each trajectory and sampling condition. This discrete set was chosen to balance numerical stability and minimal deviation from the OLS estimate. The margin used in this pre-CLIE SDP stage should therefore be interpreted as a conservative regularization for stabilizing a rough OLS solution on the sampled pose set, rather than as the final margin required for the accepted model.

In the present implementation, the constrained optimization in (8) was solved in MATLAB using CVX, a package for specifying and solving convex optimization problems. The SDP stage therefore acts as a conditional feasibility-restoring projection rather than as a replacement for the data-driven identification process.

C. CLIE Refinement and Final PD-Feasible Acceptance

The OLS and SDP stages provide a reduced parameter vector that is statistically plausible and screened for physical feasibility. However, they do not explicitly minimize the discrepancy between measured and simulated closed-loop torque responses. To reduce this remaining mismatch, the parameter vector is refined by closed-loop input error (CLIE) minimization. In this sense, CLIE can be interpreted as a bias-reduction step that complements the linear OLS estimate under closed-loop data conditions. Let $\tau_m(t_k)$ denote the measured joint torque vector at time t_k , and let $\tau_s(t_k; \phi)$ denote the simulated torque vector generated by the closed-loop forward-dynamics model parameterized by ϕ . Then, the CLIE estimate is defined by

$$\hat{\phi}_{\text{CLIE}} = \arg \min_{\phi} \sum_{k=1}^N \|\tau_m(t_k) - \tau_s(t_k; \phi)\|_2^2. \quad (9)$$

This formulation compensates for closed-loop effects not captured in the linear IDIM formulation.

Figure 3 illustrates the CLIE refinement stage. For a candidate parameter vector ϕ , the direct dynamic model is embedded in the same fixed FF+PD closed-loop controller used in the experiment. The simulated controller input torque $\tau_s(t_k; \phi)$ is then compared with the measured torque $\tau_m(t_k)$,

and the parameter vector is updated by nonlinear least squares so as to minimize this closed-loop torque-input error. Thus, CLIE refines the OLS/SDP estimate by reproducing the measured closed-loop realization process, rather than by fitting the inverse-dynamics regressor alone.

In the present framework, the simulated torque is obtained from the same reduced rigid-body model together with the fixed feedforward plus PD controller used for realization of the experimental motions. The forward-dynamics simulation used in CLIE is based on the OpenSYMORO direct dynamic model output `ddm.txt`. Thus, the CLIE step explicitly accounts for the closed-loop realization layer introduced in Sec. III-B.

The nonlinear optimization in (9) was implemented in MATLAB using `lsqnonlin`. The optimization was initialized by the reduced parameter estimate obtained from the OLS/SDP stages, so that the nonlinear refinement starts from a statistically meaningful solution rather than from an arbitrary parameter vector. This initialization is important because CLIE-only optimization from an arbitrary or non-PD parameter vector can make the forward-dynamics simulation diverge.

In the present experiments, 93 of the 160 OLS estimates were non-PD before the conditional SDP step, as summarized in Table III. The CLIE search range was deliberately wide, about ± 100 times each initial value, with clearly positive rotor inertias such as *IA3–IA8* searched on the positive side. The objective was evaluated using torque-command records with 0.25 ms trapezoidal integration and default `lsqnonlin` settings; thus, the runtimes in Appendix A represent offline optimization cost.

Nevertheless, CLIE does not by itself guarantee practical physical feasibility over the entire joint domain. For this reason, final model acceptance is based on an all-pose positive-definiteness check of the inertia matrix:

$$\mathbf{M}(\boldsymbol{\theta}; \boldsymbol{\phi}) \succ \mathbf{0} \quad \forall \boldsymbol{\theta} \in \Theta, \quad (10)$$

or, equivalently in numerical implementation,

$$\lambda_{\min}(\mathbf{M}(\boldsymbol{\theta}; \boldsymbol{\phi})) > 0 \quad \forall \boldsymbol{\theta} \in \Theta. \quad (11)$$

In the present low-cost reduced-model setting, this criterion is used as a practical final acceptance test rather than as a complete theoretical characterization of physical consistency. While positive definiteness alone does not fully guarantee complete physical consistency, it provides a necessary and practically sufficient condition for stable forward-dynamics simulation in the present reduced-model setting. If the statistically selected CLIE solution still violates this criterion, a post-CLIE SDP rescue step is applied:

$$\begin{aligned} \hat{\boldsymbol{\phi}}_{\text{rescue}} &= \arg \min_{\boldsymbol{\phi}} \left\| \boldsymbol{\phi} - \hat{\boldsymbol{\phi}}_{\text{CLIE}} \right\|_2^2 \\ \text{s.t. } \mathbf{M}(\boldsymbol{\theta}; \boldsymbol{\phi}) &\succeq \varepsilon_{\text{PD}} \mathbf{I}, \quad \forall \boldsymbol{\theta} \in \Theta. \end{aligned} \quad (12)$$

This rescue step preserves the CLIE solution as much as possible while restoring practical physical feasibility of the final reduced model. Unlike the pre-CLIE SDP stage, this rescue is applied to a refined solution already located near the PD-feasible boundary. Therefore, the role of ε_{PD} is different here: it is not a conservative screening margin for a rough

Algorithm 1 Trajectory-wise parameter identification and acceptance pipeline. The PCA-based centrality is used as a proxy for trajectory-independent parameter consistency.

```

1: for each trajectory and sampling condition do
2:   Construct  $\mathbf{W}_{\text{all}}$  from OpenSYMORO dim.txt
3:   Compute  $\hat{\boldsymbol{\phi}}_{\text{OLS}}$  by least squares
4:   Evaluate all-pose PD of  $\hat{\boldsymbol{\phi}}_{\text{OLS}}$ 
5:   if  $\hat{\boldsymbol{\phi}}_{\text{OLS}}$  is PD then
6:     Set initial value for CLIE as  $\hat{\boldsymbol{\phi}}_{\text{OLS}}$ 
7:   else
8:     for  $\varepsilon_{\text{PD}} \in \{0.001, 0.002, 0.005, 0.01\}$  in ascending
       order do
9:       Solve the SDP projection
10:      if projected solution is PD then
11:        Set initial value for CLIE as  $\hat{\boldsymbol{\phi}}_{\text{SDP}}$ 
12:      break
13:    end if
14:  end for
15:  end if
16:  Run CLIE using lsqnonlin with the selected initial
    value
17: end for
18: Analyze the final parameter cloud by PCA
19: Select the representative candidate
20: If needed, apply post-CLIE SDP rescue

```

OLS estimate, but a minimal feasibility constraint for a high-performance CLIE solution. This difference arises because the pre-CLIE SDP stage operates on a noisy OLS estimate and therefore requires a conservative margin. In contrast, the post-CLIE solution is already close to the feasible boundary and requires only minimal correction.

The representative candidate is selected from the final CLIE parameter cloud by considering its statistical centrality in the common PCA score space together with the subsequent feasibility screening and held-out validation. In the present dataset, the AG02 candidate at the 40 ms setting was located near the center of the final CLIE cloud and provided a predictive CLIE solution, but it did not satisfy the all-pose PD criterion. Therefore, the selected candidate was subsequently corrected by the post-CLIE SDP rescue step before final validation. This procedure separates statistical representativeness in the observed parameter cloud from physical feasibility over the wider joint domain.

The complete trajectory-wise routing of OLS, conditional SDP projection, CLIE refinement, representative selection, and post-CLIE rescue is summarized in Algorithm 1.

V. EXPERIMENTAL CONDITIONS

A. Candidate Trajectory Families

The candidate identification trajectories were designed as reproducible joint-space command sequences rather than numerically optimized waveforms. Each sequence was constructed from single-joint and adjacent-two-joint primitives under practical joint-range limits, following classical accelerated test

TABLE II
STRUCTURED TRAJECTORY FAMILIES USED IN THE EXPERIMENTS.

Family	Labels	Description	Count
PA	PA01–PA11	Primitive trajectories at Posture A; standard PD-stress configuration.	11
PB	PB01–PB11	Primitive trajectories at Posture B; moderate PD-stress configuration.	11
PC	PC01–PC11	Primitive trajectories at Posture C; severe PD-stress configuration.	11
AP	AP01–AP05	Adjacent-pair-only trajectories: AP01–AP03 use Postures A/B/C, and AP04–AP05 add Posture-C speed variants.	5
AG	AG01–AG02	Aggregated trajectories formed by concatenating multiple primitives.	2
V	V01–V03	Held-out multi-axis validation trajectories.	3

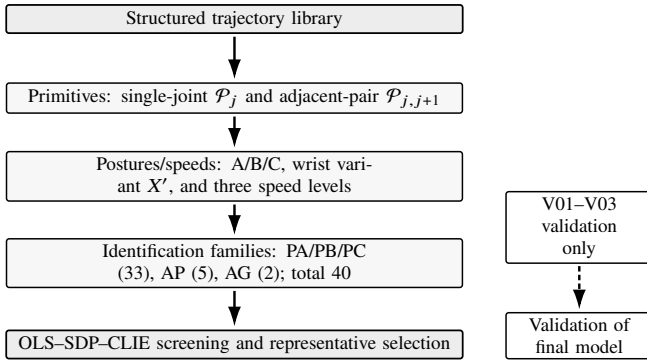


Fig. 4. PA, PB, PC, AP, and AG form 40 identification candidates; V01–V03 are reserved for validation.

motions [8] while respecting the execution constraints of CRANE-X7.

The PA, PB, and PC families use the same primitive structure at Postures A, B, and C, respectively, with increasing severity for the inertia-matrix positive-definiteness (PD) audit; selected segments also set Joint 6 to approximately 90° as a wrist-posture variant. Table II and Fig. 4 summarize the 40 identification candidates, and Appendix B gives the explicit primitives, posture vectors, and speed factors. AG02 lasts about 110 s, whereas the final all-pose PD audit uses a broader 7-DoF domain: $[-90^\circ, 90^\circ]$ for joints 1–3 and 5–7 and $[-180^\circ, 0^\circ]$ for joint 4. The numerical record is provided in Appendix A.

B. Repeated Trials and Preprocessing Conditions

Each candidate trajectory was executed repeatedly under the same controller and logging conditions. The measured data were processed by time-axis correction, anti-alias filtering, and resampling to effective sampling intervals of 10, 20, 40, and 80 ms. For each interval, only the target-grid samples were retained. Off-grid samples were not reused as phase-shifted training records because doing so added highly correlated samples and tended to worsen regressor conditioning. The preferred interval was not fixed beforehand but determined from routing behavior, cloud contraction, representative selection, and final acceptance.

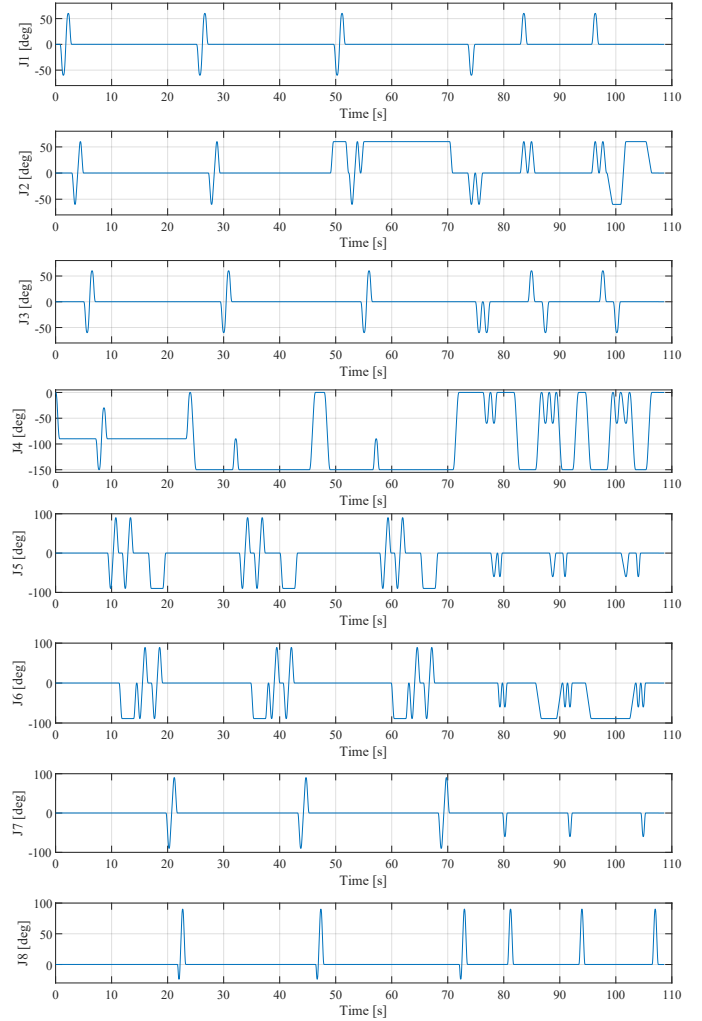


Fig. 5. Reference commands of AG02, the selected representative aggregated trajectory.

C. Validation Conditions

The held-out validation trajectories V01–V03 were kept separate from the 40 identification candidates. They combine simultaneous seven-arm-joint plus hand-axis motions and four-arm-joint-group plus hand-axis motions. Only V03 is shown qualitatively in Fig. 6; quantitative results are summarized in Table VII.

VI. RESULTS

The proposed framework is evaluated through parameter-cloud evolution, representative selection, final PD rescue, and held-out validation.

A. PCA-Based Evolution of the Parameter Clouds

Figure 7 projects the 39-dimensional parameter vectors onto a common PCA basis. The cloud becomes progressively more concentrated from OLS to SDP and further to CLIE, indicating that the staged pipeline reduces trajectory-dependent dispersion.

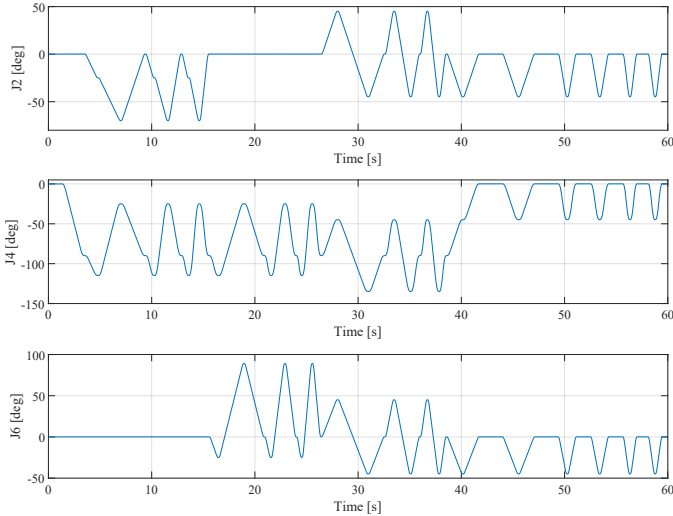


Fig. 6. Held-out validation trajectory V03. Representative commands of J2, J4, and J6 are shown.

TABLE III
ROUTING SUMMARY BEFORE CLIE REFINEMENT.

T_s [ms]	PD-OLS \rightarrow CLIE	NPD-OLS \rightarrow SDP \rightarrow CLIE	Total
10	6	34	40
20	14	26	40
40	22	18	40
80	25	15	40

The refinement is not purely contractive. AP01 remains separated from the main cloud after CLIE, suggesting a trajectory-specific solution under weak excitation because adjacent pairs are excited sequentially with limited multi-joint overlap. Thus, AP01 is not invalid but provides a useful low-excitation reference. The full record underlying Fig. 7, including κ , PD outcome, routing, ε_{PD} , and CLIE runtime, is compiled in Appendix A.

B. Representative Candidate Selection, Routing, and PD Rescue

Each OLS solution was first audited for all-pose PD. PD solutions were passed directly to CLIE, whereas non-PD solutions were projected by SDP before CLIE. Tables III and IV summarize the routing and compare AP01 with AG02 using the regressor condition number $\kappa(\mathbf{W}_{all}) = \sigma_{\max}(\mathbf{W}_{all})/\sigma_{\min}(\mathbf{W}_{all})$, route, and SDP margin. Here, O-C and O-S-C denote OLS \rightarrow CLIE and OLS \rightarrow SDP \rightarrow CLIE, respectively, and a dash in ε_{PD} means that the OLS solution was already PD and the SDP projection was skipped.

The accepted representative model was obtained from AG02 at 40 ms. Its transition through NPD-OLS, NPD-SDP, CLIE, and PD-rescue is summarized in Table V. Although the CLIE solution is statistically central and predictive, it fails the all-pose PD criterion; therefore, a post-CLIE SDP rescue was applied. Table VI shows that the correction is localized, supporting the interpretation of the rescue as a small feasibility-restoring modification.

TABLE IV
COMPARISON OF THE ADJACENT-PAIR TRAJECTORY AP01 AND THE REPRESENTATIVE CANDIDATE AG02. A DASH IN ε_{PD} INDICATES THAT THE OLS SOLUTION WAS ALREADY PD AND THE SDP PROJECTION WAS SKIPPED.

T_s [ms]	AP01			AG02		
	κ	Route	ε_{PD}	κ	Route	ε_{PD}
10	47.1	O-S-C	0.005	33.4	O-S-C	0.001
20	46.1	O-C	–	33.2	O-S-C	0.001
40	46.2	O-C	–	33.3	O-S-C	0.001
80	47.2	O-C	–	34.1	O-C	–

TABLE V
STAGE-WISE EVOLUTION OF THE REPRESENTATIVE CANDIDATE AG02.

Stage	PD	Route	ε_{PD}	Remark
Non-PD (OLS)	No	–	–	Initial estimate from OLS
Non-PD (SDP)	Yes	O-S-C	0.001	Feasible projection before CLIE
CLIE	No	–	–	Statistically central but non-PD
PD-rescue	Yes	–	0.0	Final accepted model

C. Validation on Held-Out Trajectories

After representative selection and PD rescue, the final model was evaluated on V01–V03, which were not used for identification or representative selection. Table VII shows that the rescued model preserves the root-mean-square error (RMSE) and mean normalized error (MNE) of the representative CLIE solution.

Only the most comprehensive trajectory V03 is shown qualitatively. Figure 6 shows its representative commands, and Fig. 8 compares measured and predicted torques for J2, J4, and J6. The agreement is good for J2 and J4; for J6 the absolute error remains small despite the smaller torque magnitude. Thus, the final feasibility-restoring correction does not materially degrade predictive performance.

VII. DISCUSSION

A. Reduced Modeling and Identifiability in the Low-Cost Setting

The reduction from the original 65-parameter rigid-body model to the 39-parameter model is motivated by the sensing, communication, and drivetrain constraints of CRANE-X7. Retaining all nominal rigid-body parameters may amplify numerical sensitivity and obscure physical variation with noise-driven fluctuation. By removing products of inertia and working in the base-parameter space, the formulation improves conditioning while remaining expressive enough for motion realization and torque prediction. In preliminary full-model trials, the 65-parameter regressors were solvable but often had condition numbers exceeding 100; the product-of-inertia estimates were small and weakly observable, and CLIE became markedly slower. This interpretation is supported by the OLS–SDP–CLIE cloud contraction and held-out accuracy.

This emphasis on feasibility is consistent with industrial robot studies showing that physically feasible parameter sets are essential for reliable predictive modeling [33]–[35]. The

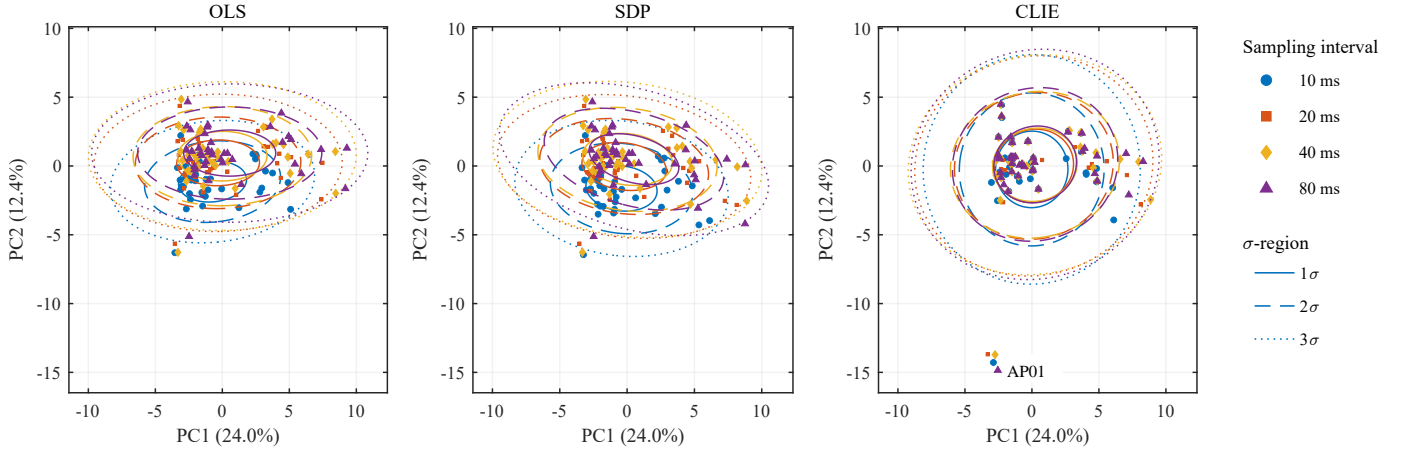


Fig. 7. PCA-based visualization of parameter clouds from OLS, SDP, and CLIE.

TABLE VI
LARGEST PARAMETER CHANGES FROM CLIE TO PD-RESCUE FOR AG02 AT THE 40 MS SETTING.

Parameter	Unit	CLIE	PD-rescue	Δ
ZZR6	$\text{kg} \cdot \text{m}^2$	-0.00014	-0.00003	0.00011
XXR4	$\text{kg} \cdot \text{m}^2$	0.00980	0.00991	-0.00011
XXR7	$\text{kg} \cdot \text{m}^2$	0.00003	0.00014	-0.00011
ZZR3	$\text{kg} \cdot \text{m}^2$	0.00163	0.00172	-0.00009
ZZR1	$\text{kg} \cdot \text{m}^2$	0.01180	0.01184	-0.00004

TABLE VII
VALIDATION METRICS ON THE HELD-OUT TRAJECTORIES V01–V03 AT THE 40 MS SETTING. RMSE: ROOT-MEAN-SQUARE ERROR; MNE: MEAN NORMALIZED ERROR.

Trajectory	CLIE RMSE	Rescue RMSE	CLIE MNE	Rescue MNE
V01	0.16761	0.16729	0.07726	0.07709
V02	0.17057	0.17032	0.08814	0.08805
V03	0.16642	0.16630	0.06721	0.06719
Mean	0.16820	0.16797	0.07753	0.07744

present contribution is complementary: feasibility-aware identification is also important for low-cost platforms, where limited sensing and delay make unconstrained high-dimensional estimation fragile.

B. Structured Excitation and PD Screening

The candidate trajectories were assembled from PA, PB, PC, AP, and AG families built from single-joint and adjacent-pair primitives rather than from numerical trajectory optimization. This favors informative, interpretable, and reproducible motions on hardware with finite resolution, realization delay, and backlash-related effects.

Classical Fourier-series excitation remains an important baseline for robot dynamic identification [20], [21], [23]. In the present platform, however, simultaneous multi-axis excitation must satisfy not only joint-position, velocity, and acceleration bounds, but also finite current/torque margins and workspace-safety constraints imposed by the hanging desktop-mounted experimental setup. Under these constraints, Fourier-series excitation design becomes a constrained nonlinear optimization

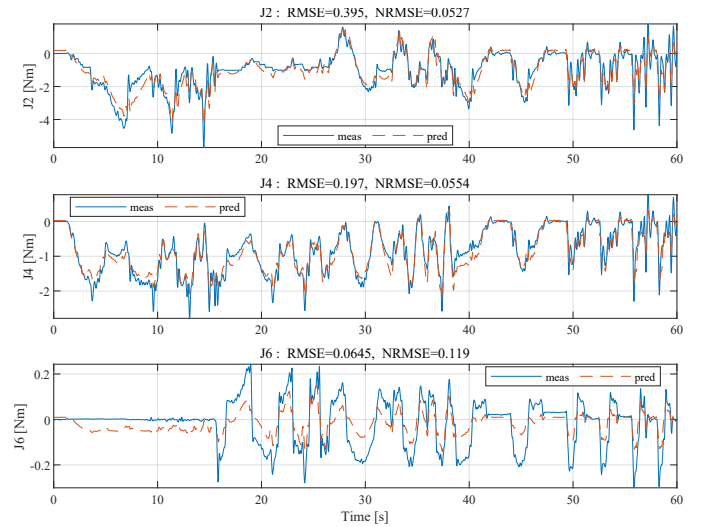


Fig. 8. Validation torque prediction on V03 for J2, J4, and J6.

problem rather than a simple condition-number minimization. The structured primitive trajectories used here were therefore chosen as a reproducible and interpretable alternative that limits excitation to single-joint and adjacent-joint groups while still producing a sufficiently well-conditioned regressor and a physically acceptable final model.

The results show that statistical representativeness and physical feasibility are different criteria. A statistically central CLIE solution can still fail the wider all-pose PD test because centrality is defined over observed data, whereas feasibility must hold over a broader domain. The all-pose PD audit therefore acts as a practical acceptance criterion; pre-CLIE SDP regularizes rough OLS solutions, whereas post-CLIE rescue minimally corrects a refined boundary-near solution.

C. Implications and Limitations

Useful dynamic modeling for low-cost robot arms does not necessarily require a maximally detailed physical model or a fully optimized excitation design. What is needed is a staged framework matched to the platform: OLS gives a

transparent baseline, SDP restores feasibility when needed, CLIE improves closed-loop predictive consistency, and the final PD audit ensures acceptance over a wider pose domain.

The small negative final entries for $ZZR6$ and $ZZ7$ in Appendix A should not be interpreted as independent physical principal moments. The model is expressed in the Open-SYMORO base-parameter space, where entries are grouped quantities; for example, $ZZR6 = YY7 + ZZ6$. Hence, the relevant test is not the sign of an individual base entry but the all-pose PD audit of $M(\theta; \phi)$, which the accepted AG02 model passes after localized rescue.

The present model is intentionally limited: it uses only viscous friction and does not reconstruct high-frequency backlash-related internal dynamics. Future work includes richer drivetrain models and quantitative comparison with trajectory-optimization-based excitation, which can be computationally costly and can yield poorly conditioned regressors under the restricted joint range and short-duration requirements of CRANE-X7.

VIII. CONCLUSION

This paper presented a reproducible and physically feasible dynamic parameter identification framework for CRANE-X7. The approach combines OLS, SDP, and CLIE with an all-pose PD audit and, when needed, final PD rescue, using a reduced 39-parameter base-parameter model obtained by removing products of inertia.

The results showed progressive concentration of the parameter cloud from OLS to SDP and CLIE, while the final accepted model preserved high predictive accuracy on held-out validation motions. For low-cost platforms, a reproducible and physically screened reduced model can be more useful than a higher-dimensional model sensitive to noise, preprocessing, and weakly observable drivetrain effects.

APPENDIX A. SUPPLEMENTARY TABLES FOR REPRODUCIBILITY

This appendix gives the numerical reproducibility record for Sec. VI. The labels follow the main text: former I/S/C are relabeled as PA/PB/PC for Postures A/B/C, and former A/G as AP/AG.

For each trajectory–sampling pair, the A1 panels report the regressor condition number κ , the OLS PD audit result, the route before CLIE, the SDP margin ε_{PD} , and the CLIE runtime t_{CLIE} . Here, $\kappa = \sigma_{\max}(W)/\sigma_{\min}(W)$ is the 2-norm condition number of the regressor W , and the PD column indicates whether the OLS estimate passed the all-pose inertia-matrix PD audit. The route abbreviations are O-C = OLS→CLIE and O-S-C = OLS→SDP→CLIE; a dash in ε_{PD} means that the SDP step was not used. Large t_{CLIE} values reflect offline nonlinear optimization with wide parameter bounds and 0.25 ms simulation steps. The final-parameter panels list the 39-dimensional final accepted model, namely the PD-rescued representative candidate AG02 at 40 ms.

PA01–PA11 (Posture A)							PB01–PB11 (Posture B)							PC01–PC11 (Posture C)						
Tr	T_s [ms]	κ	PD	Rt	ε_{PD}	t_{CLIE} [s]	Tr	T_s [ms]	κ	PD	Rt	ε_{PD}	t_{CLIE} [s]	Tr	T_s [ms]	κ	PD	Rt	ε_{PD}	t_{CLIE} [s]
PA01	10	37.8	N	O-S-C	0.005	576	PB01	10	45.8	N	O-S-C	0.005	13443	PC01	10	39.1	N	O-S-C	0.001	7643
	20	37.5	N	O-S-C	0.001	582		20	45.7	N	O-S-C	0.005	6834		20	39.0	N	O-S-C	0.001	1425
	40	38.0	Y	O-C	–	482		40	45.9	Y	O-C	–	2962		40	39.1	N	O-S-C	0.001	5261
PA02	80	41.4	Y	O-C	–	483	80	49.4	Y	O-C	–	1906	80	39.7	Y	O-C	–	35955		
	10	34.0	N	O-S-C	0.005	1248	10	36.8	N	O-S-C	0.001	8603	10	45.5	N	O-S-C	0.010	12607		
	20	33.2	N	O-S-C	0.005	1845	20	36.6	N	O-S-C	0.002	33339	20	45.4	N	O-S-C	0.005	4829		
PA03	40	33.2	Y	O-C	–	2114	40	36.7	N	O-S-C	0.002	1523	40	45.6	Y	O-C	–	3512		
	80	33.7	Y	O-C	–	1268	80	37.3	Y	O-C	–	877	80	49.2	Y	O-C	–	1733		
	10	36.3	N	O-S-C	0.005	254	10	39.7	N	O-S-C	0.001	414	10	38.3	N	O-S-C	0.001	1882		
PA04	20	39.3	Y	O-C	–	286	20	44.3	N	O-S-C	0.001	385	20	37.9	Y	O-C	–	1025		
	40	41.2	Y	O-C	–	250	40	45.9	Y	O-C	–	305	40	38.0	Y	O-C	–	1056		
	80	42.6	Y	O-C	–	247	80	47.6	Y	O-C	–	301	80	38.7	Y	O-C	–	1234		
PA05	10	34.6	Y	O-C	–	308	10	41.3	Y	O-C	–	397	10	35.2	Y	O-C	–	1614		
	20	37.9	Y	O-C	–	312	20	47.9	Y	O-C	–	523	20	35.1	Y	O-C	–	394		
	40	39.0	Y	O-C	–	270	40	49.9	Y	O-C	–	534	40	35.2	Y	O-C	–	555		
PA06	80	41.4	Y	O-C	–	220	80	53.2	Y	O-C	–	216	80	35.8	Y	O-C	–	322		
	10	33.8	N	O-S-C	0.001	36413	10	40.7	N	O-S-C	0.005	20859	10	34.7	N	O-S-C	0.001	36622		
	20	31.7	N	O-S-C	0.001	5982	20	40.4	N	O-S-C	0.005	3619	20	34.6	N	O-S-C	0.001	3239		
PA07	40	31.6	N	O-S-C	0.001	3412	40	40.5	N	O-S-C	0.005	3705	40	34.7	N	O-S-C	0.001	2930		
	80	35.8	Y	O-C	–	1199	80	44.6	N	O-S-C	0.005	42915	80	35.2	N	O-S-C	0.001	1360		
	10	42.0	N	O-S-C	0.001	283	10	49.2	N	O-S-C	0.001	263	10	42.9	N	O-S-C	0.005	469		
PA08	20	50.1	Y	O-C	–	329	20	56.9	Y	O-C	–	220	20	42.8	Y	O-C	–	251		
	40	52.8	Y	O-C	–	283	40	59.9	Y	O-C	–	210	40	44.7	Y	O-C	–	256		
	80	55.1	Y	O-C	–	242	80	62.3	Y	O-C	–	216	80	48.0	Y	O-C	–	215		
PA09	10	107.0	N	O-S-C	0.005	615	10	121.1	N	O-S-C	0.005	2756	10	75.8	N	O-S-C	0.001	295		
	20	133.3	N	O-S-C	0.001	421	20	157.5	N	O-S-C	0.005	1386	20	107.1	N	O-S-C	0.005	352		
	40	144.8	N	O-S-C	0.010	611	40	172.2	N	O-S-C	0.005	2388	40	125.1	N	O-S-C	0.001	1011		
PA10	80	154.8	N	O-S-C	0.010	425	80	182.5	N	O-S-C	0.005	2027	80	135.5	N	O-S-C	0.010	410		
	10	39.4	N	O-S-C	0.001	347	10	47.7	Y	O-C	–	231	10	41.4	Y	O-C	–	226		
	20	47.9	Y	O-C	–	294	20	58.9	Y	O-C	–	181	20	41.4	Y	O-C	–	311		
PA11	40	51.3	Y	O-C	–	253	40	62.4	Y	O-C	–	181	40	42.7	Y	O-C	–	180		
	80	54.4	Y	O-C	–	191	80	65.9	Y	O-C	–	185	80	45.9	Y	O-C	–	222		
	10	84.1	N	O-S-C	0.001	1912	10	102.8	N	O-S-C	0.001	2392	10	72.0	N	O-S-C	0.001	986		
AP01	20	124.6	N	O-S-C	0.001	835	20	152.3	Y	O-C	–	1172	20	103.1	N	O-S-C	0.001	1305		
	40	143.1	N	O-S-C	0.005	1539	40	169.9	Y	O-C	–	608	40	123.7	N	O-S-C	0.001	30883		
	80	155.5	N	O-S-C	0.005	1307	80	182.8	N	O-S-C	0.010	998	80	134.7	N	O-S-C	0.001	1368		
AG01	10	37.3	N	O-S-C	0.005	1524	10	46.4	N	O-S-C	0.005	8428	10	40.1	N	O-S-C	0.001	786		
	20	37.1	N	O-S-C	0.001	5826	20	46.3	N	O-S-C	0.005	236	20	40.0	N	O-S-C	0.001	5233		
	40	39.8	N	O-S-C	0.001	834	40	48.1	Y	O-C	–	190	40	40.1	N	O-S-C	0.001	3624		
AG02	80	44.2	N	O-S-C	0.001	1044	80	53.4	Y	O-C	–	188	80	42.8	N	O-S-C	0.001	3832		
	10	85.8	N	O-S-C	0.010	9794	10	80.6	N	O-S-C	0.001	42199	10	70.1	N	O-S-C	0.001	1752		
	20	120.1	N	O-S-C	0.010	33779	20	113.6	N	O-S-C	0.005	1241	20	96.9	N	O-S-C	0.001	6912		
AG03	40	148.1	N	O-S-C	0.005	1168	40	138.6	N	O-S-C	0.005	3152	40	120.1	N	O-S-C	0.001	1368		
	80	173.3	N	O-S-C	0.005	1601	80	159.7	N	O-S-C	0.005	1566	80	130.8	N	O-S-C	0.001	4417		

AP01–AP05, AG01–AG02						
Tr	T_s [ms]	κ	PD	Rt	ε_{PD}	t_{CLIE} [s]
AP01	10	47.1	N	O-S-C	0.005	469
	20	46.1	Y	O-C	–	548
	40	46.2	Y	O-C	–	575
AP02	80	47.2	Y	O-C	–	1683
	10	49.2	N	O-S-C	0.005	2938
	20	48.8	N	O-S-C	0.005	2253
AP03	40	48.9	N	O-S-C	0.005	1684
	80	50.0	N	O-S-C	0.005	1693
	10	42.7	Y	O-C	–	343
AP04	20	42.6	Y	O-C	–	299
	40	42.7	Y	O-C	–	235
	80	43.5	Y	O-C	–	237
AP05	10	88.3	N	O-S-C	0.001	1220
	20	88.2	N	O-S-C	0.001	554
	40	102.0	N	O-S-C	0.001	447
AG01	80	113.3	N	O-S-C	0.010	976
	10	49.3	N	O-S-C	0.001	167
	20	49.0	N	O-S-C	0.001	167
AG02	40	49.2	Y	O-C	–	138
	80	50.0	Y	O-C	–	132
	10	38.5	N	O-S-C	0.001	10743
AG03	20	38.0	N	O-S-C	0.001	2604
	40	38.1	Y	O-C	–	38648
	80	38.8	Y	O-C	–	626
AG04	10	33.4	N	O-S-C	0.001	8113
	20	33.2	N	O-S-C	0.001	3259
	40	33.3	N	O-S-C	0.001	17458
AG05	80	34.1	Y	O-C	–	1838

Final parameters (1/2)		
Param	Unit	Value
ZZR1	kg · m ²	0.01184
XXR2	kg · m ²	0.05882
ZZR2	kg · m ²	0.09040
MX2	kg · m	0.00712
MYR2	kg · m	-0.23800
XXR3	kg · m ²	0.00180
ZZR3	kg · m ²	0.00172
MX3	kg · m	0.00962
MYR3	kg · m	0.00110
XXR4	kg · m ²	0.00991
ZZR4	kg · m ²	0.02530
MX4	kg · m	0.00366
MYR4	kg · m	-0.14297
IA3	kg · m ²	0.00713
IA4	kg · m ²	0.01270
IA5	kg · m ²	0.00414
IA6	kg · m ²	0.00373
IA7	kg · m ²	0.00448
IA8	kg · m ²	0.00499

Final parameters (2/2)		
Param	Unit	Value
XXR5	kg · m ²	0.01560
ZZR5	kg · m ²	0.00024
MX5	kg · m	-0.00206
MYR5	kg · m	0.00137
XXR6	kg · m ²	0.00083
ZZR6	kg · m ²	-0.00003
MX6	kg · m	0.00130
MYR6	kg · m	-0.00522
XXR7	kg · m ²	0.00014
ZZ7	kg · m ²	-0.00003
MX7	kg · m	-0.00034
MZ7	kg · m	-0.00005
FV1	N · m · s/rad	0.07360
FV2	N · m · s/rad	0.31700
FV3	N · m · s/rad	0.07070
FV4	N · m · s/rad	0.24700
FV5	N · m · s/rad	0.02870
FV6	N · m · s/rad	0.04590
FV7	N · m · s/rad	0.03310
FV8	N · m · s/rad	0.03130

APPENDIX B. TRAJECTORY GENERATION

The identification trajectories were generated as joint-space waypoint sequences, not as optimized continuous waveforms. Each waypoint-to-waypoint segment was interpolated by a standard point-to-point joint-space trajectory with a continuous acceleration profile and, when allowed by the segment length, a constant-velocity phase. The trajectory design itself is therefore specified by the nominal posture, the active joint set, the amplitude, the sign pattern, and the speed level.

For a nominal posture \bar{q} , the single-joint primitive for joint j is

$$\mathcal{P}_j(a_j; \bar{q}) : \bar{q} \rightarrow \bar{q} - a_j e_j \rightarrow \bar{q} + a_j e_j \rightarrow \bar{q},$$

where e_j is the unit vector of joint j . Thus, its commanded offset sequence is $0^\circ \rightarrow -a_j \rightarrow +a_j \rightarrow 0^\circ$. For an adjacent two-joint primitive, define

$$\delta_{j,j+1} = s_j a_j e_j + s_{j+1} a_{j+1} e_{j+1}, \quad s_j, s_{j+1} \in \{-1, +1\}.$$

Then the primitive is compactly written as

$$\mathcal{P}_{j,j+1}(\delta_{j,j+1}; \bar{q}) : \bar{q} \rightarrow \bar{q} - \delta_{j,j+1} \rightarrow \bar{q} + \delta_{j,j+1} \rightarrow \bar{q}.$$

The sign pair (s_j, s_{j+1}) specifies the in-phase or opposite-phase adjacent-joint excitation.

The following posture vectors are defined in the eight-axis command space, where the first seven components correspond to the arm joints and the eighth component corresponds to the hand axis. The posture-based families PA, PB, and PC use the same primitive structure but different nominal postures:

$$\begin{aligned} \bar{q}_A &= [0, 0, 0, -90, 0, 0, 0, 0]^\circ, \\ \bar{q}_B &= [0, 0, 0, -150, 0, 0, 0, 0]^\circ, \\ \bar{q}_C &= [0, 60, 0, -150, 0, 0, 0, 0]^\circ. \end{aligned}$$

Selected segments also use the wrist variant

$$\bar{q}_{X'} = \bar{q}_X + 90^\circ e_6, \quad X \in \{A, B, C\},$$

to include a more severe wrist configuration in the PD audit. The relative speed factor used in the trajectory generator is normally selected from $\{0.30, 0.60, 0.90\}$. For proximal or large-amplitude motions, the factors are reduced to $\{0.25, 0.50, 0.75\}$ or $\{0.20, 0.40, 0.60\}$ to keep the executed motion within stable current and velocity ranges.

The PA, PB, and PC families consist of 33 trajectories in total. The main grid contains $3 \times 3 \times 3 = 27$ trajectories, corresponding to three postures, three primitive-combination patterns, and three speed levels. In addition, two concatenated trajectories are included for each posture, giving $(1 + 1) \times 3 = 6$ trajectories. Equivalently, each posture family contains nine grid trajectories and two concatenated trajectories, i.e., $9 + 2 = 11$. Together with five adjacent-pair-only trajectories AP01–AP05 and two aggregated trajectories AG01–AG02, the complete identification set contains $33 + 5 + 2 = 40$ trajectories.

AP01–AP03 apply the high-speed adjacent-pair-only primitive at Postures A, B, and C, respectively, while AP04–AP05 use Posture C as additional speed variants of the adjacent-pair-only primitive. AG01 connects three adjacent-pair primitives, whereas AG02 connects three single-joint

and three adjacent-pair primitives. The validation family V consists of independent multi-axis motions and was not used for parameter estimation.

REFERENCES

- [1] T. Z. Zhao, V. Kumar, S. Levine, and C. Finn, "Learning fine-grained bimanual manipulation with low-cost hardware," in *Robotics: Science and Systems*, Daegu, Korea, Jul. 2023.
- [2] ALOHA 2 Team, J. Aldaco, T. Armstrong, R. Baruch, J. Bingham, S. Chan, K. Draper, D. Dwibedi, C. Finn, P. Florence, S. Goodrich, W. Gramlich, T. Haarnoja, A. Herzog, J. Hoech, T. Nguyen, I. Pierson, T. Wahrburg, L. Wang, S. Young, Y. Lu, and S. Levine, "Aloha 2: An enhanced low-cost hardware for bimanual teleoperation," *arXiv preprint*, arXiv:2405.02292 [cs.RO], Feb. 2024.
- [3] RT Corporation, "CRANE-X7," <https://rt-net.jp/products/crane-x7/>.
- [4] ROBOTIS, "DYNAMIXEL X-Series e-Manual," Online, 2026, available: ROBOTIS e-Manual.
- [5] K. Yamane, Y. Saigusa, S. Sakaino, and T. Tsuji, "Soft and rigid object grasping with cross-structure hand using bilateral control-based imitation learning," *IEEE Robotics and Automation Letters*, vol. 9, no. 2, pp. 1198–1205, Feb. 2024.
- [6] K. Inami, S. Sakaino, and T. Tsuji, "Motion retouch: Motion modification using four-channel bilateral control," in *Proceedings of the 2025 IEEE International Conference on Mechatronics*, Wollongong, Australia, Feb. 2025, pp. 1–6.
- [7] K. Yamane, Y. Li, M. Konosu, K. Inami, J. Oaki, S. Sakaino, and T. Tsuji, "Design and experimental validation of sensorless 4-channel bilateral teleoperation for low-cost manipulators," *arXiv preprint*, arXiv:2507.06174 [cs.RO], Jul. 2025.
- [8] H. Mayeda, K. Osuka, and A. Kangawa, "A new identification method for serial manipulator arms," in *IFAC Proceedings Volumes*, vol. 17, no. 2, Jul. 1984, pp. 2429–2434.
- [9] H. Mayeda, K. Yoshida, and K. Osuka, "Base parameters of manipulator dynamic models," *IEEE Transactions on Robotics and Automation*, vol. 6, no. 3, pp. 312–321, Jun. 1990.
- [10] M. Gautier and W. Khalil, "Direct calculation of minimum set of inertial parameters of serial robots," *IEEE Transactions on Robotics and Automation*, vol. 6, no. 3, pp. 368–373, Jun. 1990.
- [11] K. Yoshida and W. Khalil, "Verification of the positive definiteness of the inertial matrix of manipulators using base inertial parameters," *The International Journal of Robotics Research*, vol. 19, no. 5, pp. 498–510, May 2000.
- [12] C. D. Sousa and R. Cortesão, "Physical feasibility of robot base inertial parameter identification: A linear matrix inequality approach," *The International Journal of Robotics Research*, vol. 33, no. 6, pp. 931–944, Feb. 2014.
- [13] P. M. Wensing, S. Kim, and J.-J. E. Slotine, "Linear matrix inequalities for physically consistent inertial parameter identification: A statistical perspective on the mass distribution," *IEEE Robotics and Automation Letters*, vol. 3, no. 1, pp. 60–67, Jan. 2018.
- [14] M. Gautier, A. Janot, and P.-O. Vandanjon, "A new closed-loop output error method for parameter identification of robot dynamics," *IEEE Transactions on Control Systems Technology*, vol. 21, no. 2, pp. 428–444, Mar. 2013.
- [15] A. Perrusquía, R. Garrido, and W. Yu, "Stable robot manipulator parameter identification: A closed-loop input error approach," *Automatica*, vol. 141, 110294, Jul. 2022.
- [16] Q. Leboutet, J. Roux, A. Janot, J. R. Guadarrama-Olvera, and G. Cheng, "Inertial parameter identification in robotics: A survey," *Applied Sciences*, vol. 11, no. 9, 4303, May 2021.
- [17] W. Khalil, A. Vijayalingam, B. Khomutenko, I. Mukhanov, P. Lemoine, and G. Ecorchard, "Opensymoro: An open-source software package for symbolic modelling of robots," in *Proceedings of the 2014 IEEE/ASME International Conference on Advanced Intelligent Mechatronics*, Besancon, France, Jul. 2014, pp. 1206–1211.
- [18] W. Khalil and E. Dombre, *Modeling, Identification and Control of Robots*. London, UK: Hermes Penton Science, 2002.
- [19] C. G. Atkeson, C. H. An, and J. M. Hollerbach, "Estimation of inertial parameters of manipulator loads and links," *The International Journal of Robotics Research*, vol. 5, no. 3, pp. 101–119, Sep. 1986.
- [20] J. Swevers, C. Ganseman, J. De Schutter, and H. Van Brussel, "Experimental robot identification using optimised periodic trajectories," *Mechanical Systems and Signal Processing*, vol. 10, no. 5, pp. 561–577, Sep. 1996.

- [21] J. Swevers, C. Ganseman, D. B. Tukel, J. De Schutter, and H. Van Brussel, "Optimal robot excitation and identification," *IEEE Transactions on Robotics and Automation*, vol. 13, no. 5, pp. 730–740, Oct. 1997.
- [22] C. Presse and M. Gautier, "New criteria of exciting trajectories for robot identification," in *Proceedings of the 1993 IEEE International Conference on Robotics and Automation*, Atlanta, Georgia, May 1993, pp. 907–912.
- [23] K.-J. Park, "Fourier-based optimal excitation trajectories for the dynamic identification of robots," *Robotica*, vol. 24, no. 5, pp. 625–633, Mar. 2006.
- [24] J. Wu, J. Wang, and Z. You, "An overview of dynamic parameter identification of robots," *Robotics and Computer-Integrated Manufacturing*, vol. 26, no. 5, pp. 414–419, Oct. 2010.
- [25] V. Mata, F. Benimeli, N. Farhat, and A. Valera, "Dynamic parameter identification in industrial robots considering physical feasibility," *Advanced Robotics*, vol. 19, no. 1, pp. 101–119, Apr. 2005.
- [26] J. Jin and N. Gans, "Parameter identification for industrial robots with a fast and robust trajectory design approach," *Robotics and Computer-Integrated Manufacturing*, vol. 31, pp. 21–29, Feb. 2015.
- [27] C. D. Sousa and R. Cortesão, "Inertia tensor properties in robot dynamics identification: A linear matrix inequality approach," *IEEE/ASME Transactions on Mechatronics*, vol. 24, no. 1, pp. 406–411, Feb. 2019.
- [28] Z. Fu, J. Pan, E. Spyrakos-Papastavridis, Y.-H. Lin, X. Zhou, X. Chen, and J. S. Dai, "A lie-theory-based dynamic parameter identification methodology for serial manipulators," *IEEE/ASME Transactions on Mechatronics*, vol. 26, no. 5, pp. 2688–2699, Oct. 2021.
- [29] V. A. Sujan and S. Dubowsky, "An optimal information method for mobile manipulator dynamic parameter identification," *IEEE/ASME Transactions on Mechatronics*, vol. 8, no. 2, pp. 215–225, Jun. 2003.
- [30] M. Díaz-Rodríguez, Á. Valera, V. Mata, and M. Vallés, "Model-based control of a 3-dof parallel robot based on identified relevant parameters," *IEEE/ASME Transactions on Mechatronics*, vol. 18, no. 6, pp. 1737–1744, Dec. 2013.
- [31] J. Swevers, W. Verdonck, and J. De Schutter, "Dynamic model identification for industrial robots," *IEEE Control Systems Magazine*, vol. 27, no. 5, pp. 58–71, Oct. 2007.
- [32] A. Janot and P. M. Wensing, "Sequential semidefinite optimization for physically and statistically consistent robot identification," *Control Engineering Practice*, vol. 107, 104699, Feb. 2021.
- [33] C. Gaz, M. Cognetti, A. Oliva, P. R. Giordano, and A. D. Luca, "Dynamic identification of the franka emika panda robot with retrieval of feasible parameters using penalty-based optimization," *IEEE Robotics and Automation Letters*, vol. 4, no. 4, pp. 4147–4154, Oct. 2019.
- [34] T. Xu, J. Fan, Y. Chen, X. Ng, J. Marcelo H. Ang, Q. Fang, Y. Zhu, and J. Zhao, "Dynamic identification of the kuka lbr iiwa robot with retrieval of physical parameters using global optimization," *IEEE Access*, vol. 8, pp. 108 018 – 108 031, Jun. 2020.
- [35] Y. Huang, J. Ke, X. Zhang, and J. Ota, "Dynamic parameter identification of serial robots using a hybrid approach," *IEEE Transactions on Robotics*, vol. 39, no. 2, pp. 1607–1621, Apr. 2023.
- [36] Y. Wang, R. Gondokaryono, A. Munawar, and G. S. Fischer, "A convex optimization-based dynamic model identification package for the da vinci research kit," *IEEE Robotics and Automation Letters*, vol. 4, no. 4, pp. 3657–3664, Oct. 2019.